Inverse design of mechanical springs with tailored nonlinear elastic response utilizing internal contact

Bluhm, Gore Lukas; Sigmund, Ole; Poulios, Konstantinos

Published in:
International Journal of Non-Linear Mechanics

Link to article, DOI:
10.1016/j.ijnonlinmec.2023.104552

Publication date:
2023

Document Version
Publisher's PDF, also known as Version of record

International Journal of Non–Linear Mechanics 157 (2023) 104552

Contents lists available at ScienceDirect

International Journal of Non-Linear Mechanics

journal homepage: www.elsevier.com/locate/nlm

Inverse design of mechanical springs with tailored nonlinear elastic response utilizing internal contact

Gore Lukas Bluhm, Ole Sigmund, Konstantinos Poulios *

Department of Civil and Mechanical Engineering, Technical University of Denmark, Koppels Allé, Building 404, 2800 Kgs. Lyngby, Denmark

ARTICLE INFO

Keywords:
Topology optimization
Non-linear spring
Contact mechanics
Inverse design

ABSTRACT

This work employs a contact-aware topology optimization approach for the design of nonlinear springs with a broad range of prescribed load–displacement responses in both tension and compression. By leveraging the third medium contact approach to model internal contact, this method enables the utilization of collision between parts to achieve the desired load–displacement response while minimizing material consumption. The effectiveness of the proposed computational design approach is demonstrated using axially loaded springs as a benchmark, but the proposed method is also applicable to more general cases, including the design of periodic nonlinear material microstructures and metamaterials.

1. Introduction

Designing structures or periodic microstructures and metamaterials with tailored elastic load-deformation responses is essential in various technical applications like footwear, prosthetics, micro-electro-mechanical devices, among many others. The case of axially loaded nonlinear springs, in particular, provides in its simplicity an excellent benchmark for demonstrating how computational design methods can lead to improved performance in such applications. In this context, the present work employs contact-aware topology optimization for designing nonlinear springs with a broad range of prescribed nonlinear responses in both tension and in compression.

Topology optimization in general, albeit without modeling of internal contact, has been used in the past for solving similar inverse design problems. Periodic nonlinear material microstructures have been among other optimized with regard to desired stress–strain curves [1], target tangent stiffness [2] or a desired auxetic behavior [3–5]. Independent of the specific objective, all these models are based on unit cells with periodic boundary conditions. Typically, a homogenized strain history is prescribed in one specific direction and the objective is formulated in terms of homogenized stress or stiffness in the same direction, or as homogenized stress or strain in the transverse direction. Among these two possibilities, the former one is rather similar to the case of axially loaded strings, addressed in the present work.

Another related inverse design problem, where topology optimization has proved very successful, is the design of compliant mechanisms. Nonlinear compliant mechanisms, which to a large degree resemble the nonlinear spring design pursued in the present work, have already been treated with topology optimization more than two decades ago [6–8]. These systems are usually slightly more complex than springs in the sense that they involve non-coinciding input and output regions, where the mechanism is actuated and where the objective is evaluated, respectively. Moreover the actuation is not always a force or a prescribed displacement, but it can also be a heat source, or piezoelectric material, etc. [9,10].

The inverse design of nonlinear springs, has been treated in [11] using curved beam elements for large deformations and a genetic algorithm. Bending dominated designs were produced, tailored against a desired nonlinear response which was either stiffening, or softening, or a combination of the two. More recently, topology optimization has been successfully used to synthesize nonlinear springs consisting of two different elastomer materials tailored against prescribed load-displacement functions [12]. This method has also been applied to the aforementioned field of nonlinear material microstructures in three dimensions [13].

Major difficulties in the inverse design of nonlinear springs stem from the large deformations involved, which lead to strong geometric nonlinearities and possible collision between parts of the structure. Moreover, the inverse design problem does not have a unique solution. Very dissimilar spring shapes can produce very similar responses. For this reason, adding a small volume penalization, as suggested in [12], is essential for formulating a well-posed optimization problem. In this manner, among all possible spring geometries that can satisfy the prescribed response, the one with minimal material usage is prioritized. The main contribution of the present work is to include the modeling of internal contact in the inverse design process, based on the third

* Corresponding author.
E-mail address: kopo@dtu.dk (K. Poulios).

https://doi.org/10.1016/j.ijnonlinmec.2023.104552
Received 13 July 2023; Received in revised form 9 September 2023; Accepted 16 September 2023
Available online 23 September 2023

medium contact approach [14–16]. By this, collision between parts of the design, is not only accounted for, but can also be exploited to achieve desired more advanced load–displacement responses with as little material as possible.

Section 2 summarizes the contact-aware topology optimization framework from [15], which serves as the foundation of the present study. Section 3 includes the main results of the present work, a collection of elastomer spring designs optimized against stiffening or softening response in compression and in tension, or even for a combination of different requirements for compression and tension. An overall evaluation of the proposed method as well as some concluding remarks are provided in Section 4.

2. Methods

The topology optimization framework from [15] constitutes the foundation of the present work, however with some adaptations and improvements described in the following subsections. The main advantage of this framework is that it provides a self-contained topology optimization model entirely defined in the continuous setting, prior to any discretization. For an implementation of the third medium contact method in a more conventional topology optimization framework, the reader is referred to [16].

2.1. Notational conventions

A somewhat special syntax is used for directional derivatives, explained with the following two examples

$$A_{,b}\,(a,b,c\,;\beta) \quad \text{and} \quad A_{,b,a}\,(a,b,c\,;\beta\,;\alpha)\,.$$

The first expression denotes the directional derivative of a quantity A with respect to b in the direction β. The second expression is a second order derivative with respect to b and a in directions β and α, respectively.

The $\mathbb{H}$ operator is used for denoting second spatial derivatives, i.e. Hessians, of scalar and vector fields, respectively defined as

$$\mathbb{H}a = \frac{\partial^2 a}{\partial X_i \partial X_j} \quad \text{and} \quad \mathbb{H}b = \frac{\partial^2 b_i}{\partial X_j \partial X_k},$$

for a scalar field a and a vector field b. The indices i, j, and k, correspond to the first, second, and possibly third dimension of the resulting tensor and X is the position vector in the reference configuration.

Last, the operator $\langle t\rangle_{[a,b]}$ is used to express the linear activation function between values a and b. Its exact definition is

$$\langle t\rangle_{[a,b]} = \begin{cases} a & \text{if} \quad t \le a, \\ t & \text{if} \quad a < t < b, \\ b & \text{if} \quad b \le t. \end{cases}$$

2.2. Optimization problem

A scalar field χ is defined over the design domain Ω, as the design variable which describes the presence of solid material, for positive values, or the absence of it, for negative values. The load history of the structure can be described by means of a series of N prescribed displacements imposed on part of the domain boundary $\partial\Omega$. For example, a set of scalar valued displacements $d^{\langle j\rangle}$ for $j = 1\dots N$, can be imposed on the top side Γ_T of the design domain shown in Fig. 1. For each displacement value $d^{\langle j\rangle}$ in the loading history, a respective displacement field $(u_x^{\langle j\rangle}, u_y^{\langle j\rangle})$ is defined as a vector field variable $\boldsymbol{u}^{\langle j\rangle}$ on Ω, which one has to solve for. Moreover, a set of scalar multipliers $q^{\langle j\rangle}$ are used for imposing the prescribed displacements $d^{\langle j\rangle}$. Each multiplier $q^{\langle j\rangle}$ represents the reaction force due to the respective imposed displacement $d^{\langle j\rangle}$. In total, the set of all control points $\{d^{\langle j\rangle}, q^{\langle j\rangle}\}$ defines the actual loading path for the structure, that is to be optimized against a target response.

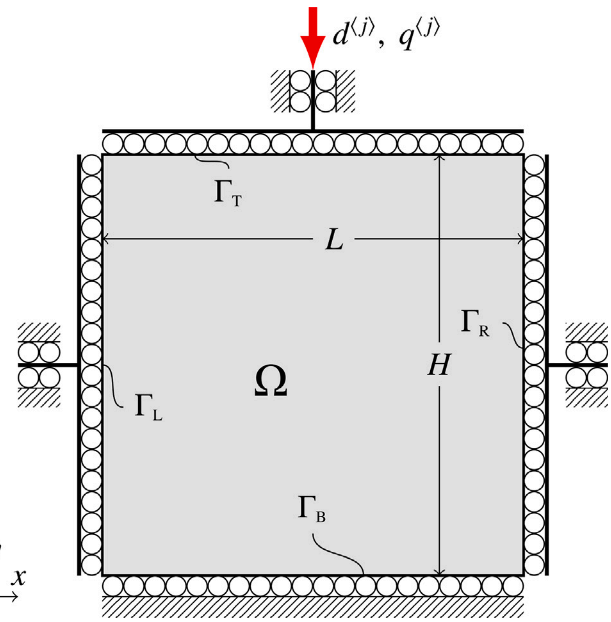

Fig. 1. Rectangular design domain Ω of length L and height H with boundaries Γ_L, Γ_B, Γ_R, Γ_T. The design is assumed to have an out-of-plane thickness T. By convention, a positive displacement $d^{\langle j\rangle}$ and a positive reaction force $q^{\langle j\rangle}$ correspond to tension.

For the optimization problem, an objective function C is considered, which is a function of both the scalar multipliers $q^{\langle j\rangle}$ and the design field χ. For simplicity, the objective function is assumed to be in the additive split form

$$C = \sum_j C_q^{\langle j\rangle}\left(q^{\langle j\rangle}\right) \;+\; C_\chi(\chi). \tag{1}$$

The term $C_\chi(\chi)$ in this expression is used for penalizing the total volume of solid in the design, and hence favor designs of minimal material usage [12]. The same term is also used for controlling the steepness and the evolution of the level-set field χ during the optimization.

The following sigmoid function is used to convert the design field χ into a material density quantity

$$\rho(\chi) = \frac{1}{1+\mathrm{e}^{-\chi}}. \tag{2}$$

By its definition, ρ is bounded by the asymptotic limits 0 and 1, corresponding to void and solid material, respectively.

Standard RAMP interpolation [17] is used for penalizing nonphysical intermediate density material. Material stiffness in the domain Ω is therefore scaled by the following function of the design variable χ

$$\mathcal{E}(\chi) = \mathcal{E}_0 + \left(1-\mathcal{E}_0\right)\;\frac{\rho(\chi)}{1+p(1-\rho(\chi))}, \tag{3}$$

where p is the RAMP penalization factor and $\mathcal{E}_0$ is the material contrast between void and solid regions, that ensures a minimum residual stiffness in the void, for numerical reasons. The RAMP penalization factor $p = 8$ has been used for all examples solved in the present work.

The mechanical equilibrium of a hyperelastic material structure in Ω, can be expressed in weak form by means of an appropriate virtual work expression. Through the material interpolation Eq. (3), the weak form equation for mechanical equilibrium includes a local scaling with $\mathcal{E}(\chi)$, i.e. it is also dependent on the design variable χ, and it can hence be written as

$$\mathcal{R}^{\langle j\rangle}\left(\chi, \boldsymbol{u}^{\langle j\rangle}, q^{\langle j\rangle}\,; \delta\boldsymbol{u}^{\langle j\rangle}, \delta q^{\langle j\rangle}\right) = 0 \qquad \forall \quad \delta\boldsymbol{u}^{\langle j\rangle}, \delta q^{\langle j\rangle}, \tag{4}$$

where $\delta\boldsymbol{u}^{\langle j\rangle}$ and $\delta q^{\langle j\rangle}$ are virtual variations of $\boldsymbol{u}^{\langle j\rangle}$ and $q^{\langle j\rangle}$, respectively.

Eq. (4) defines $q^{\langle j\rangle}$ as an implicit function of χ which has to be accounted for in the minimization of the objective function from Eq. (1). Introducing adjoint variable fields $\lambda_u^{\langle j\rangle}$ and adjoint values $\lambda_q^{\langle j\rangle}$, and employing standard adjoint analysis, this implicit dependency can be incorporated in the augmented functional

$$C^* = \sum_j C_q^{\langle j\rangle}\left(q^{\langle j\rangle}\right) + \mathcal{R}^{\langle j\rangle}\left(\chi, \boldsymbol{u}^{\langle j\rangle}, q^{\langle j\rangle}; \lambda_u^{\langle j\rangle}, \lambda_q^{\langle j\rangle}\right) + C_\chi(\chi), \tag{5}$$

so that the minimization of C under the constraint Eq. (4) is equivalent to finding a stationary point of C^*. At that point, the variation of C^* with respect to $q^{\langle j\rangle}$, $\boldsymbol{u}^{\langle j\rangle}$, and χ, i.e.

$$\begin{aligned}\delta C^* = \sum_j C_{q,q}^{\langle j\rangle}\left(q^{\langle j\rangle}; \delta q^{\langle j\rangle}\right) + \mathcal{R}_{,q}^{\langle j\rangle}\left(\chi, \boldsymbol{u}^{\langle j\rangle}, q^{\langle j\rangle}; \lambda_u^{\langle j\rangle}, \lambda_q^{\langle j\rangle}; \delta q^{\langle j\rangle}\right) \\ + \sum_j \mathcal{R}_{,\boldsymbol{u}}^{\langle j\rangle}\left(\chi, \boldsymbol{u}^{\langle j\rangle}, q^{\langle j\rangle}; \lambda_u^{\langle j\rangle}, \lambda_q^{\langle j\rangle}; \delta \boldsymbol{u}^{\langle j\rangle}\right) \\ + C_{\chi,\chi}(\chi; \delta\chi) + \sum_j \mathcal{R}_{,\chi}^{\langle j\rangle}\left(\chi, \boldsymbol{u}^{\langle j\rangle}, q^{\langle j\rangle}; \lambda_u^{\langle j\rangle}, \lambda_q^{\langle j\rangle}; \delta\chi\right)\end{aligned} \tag{6}$$

is required to vanish.

The adjoint multipliers $\lambda_u^{\langle j\rangle}$ and $\lambda_q^{\langle j\rangle}$ are chosen to fulfill the adjoint equations

$$\begin{aligned}&C_{q,q}^{\langle j\rangle}(q^{\langle j\rangle}; \delta q^{\langle j\rangle}) + \\ &\mathcal{R}_{,q}^{\langle j\rangle}\left(\chi, \boldsymbol{u}^{\langle j\rangle}, q^{\langle j\rangle}; \lambda_u^{\langle j\rangle}, \lambda_q^{\langle j\rangle}; \delta q^{\langle j\rangle}\right) = 0 \quad \forall\ \delta q^{\langle j\rangle}, \\ &\mathcal{R}_{,\boldsymbol{u}}^{\langle j\rangle}\left(\chi, \boldsymbol{u}^{\langle j\rangle}, q^{\langle j\rangle}; \lambda_u^{\langle j\rangle}, \lambda_q^{\langle j\rangle}; \delta \boldsymbol{u}^{\langle j\rangle}\right) = 0 \quad \forall\ \delta \boldsymbol{u}^{\langle j\rangle},\end{aligned} \tag{7}$$

so that the first two rows in Eq. (6) vanish, and the stationary point condition, $\delta C^* = 0$, yields

$$C_{\chi,\chi}(\chi; \delta\chi) + \sum_j \mathcal{R}_{,\chi}^{\langle j\rangle}\left(\chi, \boldsymbol{u}^{\langle j\rangle}, q^{\langle j\rangle}; \lambda_u^{\langle j\rangle}, \lambda_q^{\langle j\rangle}; \delta\chi\right) = 0 \quad \forall\ \delta\chi. \tag{8}$$

In total, the coupled set of Eqs. (4), (7) and (8) constitute the entire inverse design problem. It remains to provide the specific choices for the functions $C_q^{\langle j\rangle}$ and the functionals C_χ, and $\mathcal{R}^{\langle j\rangle}$.

2.3. Load path control

The desired nonlinear response for a spring design problem is provided in terms of a number of given control points $\{d^{\langle j\rangle}, q_*^{\langle j\rangle}\}$. Each contribution $C_q^{\langle j\rangle}\left(q^{\langle j\rangle}\right)$ in the objective function is then defined as a weighted square distance between the actual load $q^{\langle j\rangle}$ and the target load $q_*^{\langle j\rangle}$, as a measure of deviation from the desired load path, i.e.

$$C_q^{\langle j\rangle}\left(q^{\langle j\rangle}\right) = \frac{w_q^{\langle j\rangle}}{2}\left\|q^{\langle j\rangle} - q_*^{\langle j\rangle}\right\|^2. \tag{9}$$

Different control points along the loading path can be weighted individually by choosing the weight constants $w_q^{\langle j\rangle}$ appropriately.

2.4. Design control and evolution

In this subsection, the dependence of the objective on the design variable χ, i.e. the functional $C_\chi(\chi)$ in Eq. (1), will be introduced. One major component in $C_\chi(\chi)$ is a penalization of the total volume of solid material used in the design, corresponding to the integral

$$V = T \cdot \int_\Omega \rho(\chi)\ d\Omega, \tag{10}$$

where T denotes the out-of-plane thickness of the 3D domain.

In total, apart from the volume penalization, the functional $C_\chi(\chi)$ contains three more components, that will be explained below, and is defined as

$$\begin{aligned}C_\chi(\chi) = T \cdot \int_\Omega\ & k_\rho\, \rho(\chi) \\ &+ \frac{k_i}{n}\left\langle \|\nabla\chi\| - 8/l_i \right\rangle^n \\ &+ \frac{k_H}{2}\mathbb{H}\chi : \mathbb{H}\chi \\ &+ \frac{\dot{\chi}^2 + l_t^2\,\|\nabla\dot{\chi}\|^2}{2}\ d\Omega.\end{aligned} \tag{11}$$

The volume penalization term in Eq. (11) is scaled with the weight constant k_ρ. Without this kind of material cost in the objective, the target load–displacement curve could in general be achieved with a multitude of distinct designs, even with designs that include intermediate gray material. Including a small volume penalization, as suggested in [12], favors a design of minimum material usage among alternative solutions with the same performance. In that sense, k_ρ should be chosen small enough so that it does not dominate the main objective, expressed in $C_q^{\langle j\rangle}$, but large enough to promote a unique and discrete design. There exists a range of values for k_ρ, for which, the resulting optimized design is rather insensitive to the choice of k_ρ.

The second term in Eq. (11), scaled with the weight constant k_i, is a penalization term that ensures that the slope of the level-set field χ will not significantly exceed the value of $8/l_i$. Due to this constraint, optimization will converge as the width of the gray material zone between solid and void decreases towards l_i. The interface width l_i, given in units of length, needs to be as small as possible but still not much smaller than the element size, so that the finite element approximation can represent the solid-void transition sufficiently. The penalization weight k_i needs to be sufficiently large to ensure that the constraint is satisfied. For a wide range of values for k_i, above a certain level, the optimization result is practically independent of the exact choice of k_i. The optimization result is also rather independent of the p-norm exponent n within a range of moderate values. The exponent $n = 6$ is used throughout all examples shown in the present work.

The third term in Eq. (11), scaled with the weight constant k_H, provides a very weak regularization of the level-set field χ in the form of a penalization of its curvature. This ensures a smooth solution in regions where the contributions from all other terms of the objective function eventually vanish. A very small weight k_H is sufficient, and for such small values, the exact choice of this regularization parameter has practically no effect on the final result.

The last term of C_χ, defined in Eq. (11), controls the evolution of the design field during optimization. It involves the rate $\dot{\chi}$ of the design field with respect to pseudo-time t, which describes the evolution of the design during optimization. This term converts the one-shot optimization formulation into an ODE based one, as proposed in [18]. At time zero, the design field χ corresponds to the initial guess, and at infinite time, the final design fulfilling the original optimality is retrieved. In all examples shown in the present work, the ODE arising due to this time dependent term, is integrated numerically until infinite time. This means that in the last time step of the numerical time integration, the last term of Eq. (11) is entirely removed. Therefore, an exact optimality point is eventually obtained without any contribution from this term. For the same reason, the diffusivity parameter l_t present in this term, is not essential for the ultimate solution, but it only affects how fast the optimization procedure moves towards high-contrast designs.

The directional derivative $C_{\chi,\chi}$, appearing in the optimality Eq. (8), can be obtained from Eq. (11) by approximating pseudo-time derivatives with a backward Euler scheme, and applying common differentiation rules. This derivation yields

$$\begin{aligned}C_{\chi,\chi}(\chi; \delta\chi) = \\ T \cdot \int_\Omega\ & k_\rho\, \rho'(\chi)\delta\chi \\ &+ k_i\left\langle \|\nabla\chi\| - 8/l_i \right\rangle^{n-1} \frac{\nabla\chi\cdot\nabla\delta\chi}{\|\nabla\chi\|} \\ &+ k_H\mathbb{H}\chi : \mathbb{H}\delta\chi \\ &+ \frac{(\chi - \chi^*)\,\delta\chi + l_t^2\,(\nabla\chi - \nabla\chi^*)\cdot\nabla\delta\chi}{\Delta t}\ d\Omega,\end{aligned} \tag{12}$$

where Δt is the pseudo-time step and χ^* is the design field in the previous time instant. With Eq. (12) substituted in Eq. (8), the latter together with Eqs. (4) and (7), provide an update of the design level-set field from $\chi^* = \chi(t - \Delta t)$ to $\chi = \chi(t)$. Ultimately, this system of equations is solved for $\Delta t = \infty$, which makes the final step independent of χ^*, and the final design $\chi(t = \infty)$ is obtained.

2.5. Mechanical model

The last model component to be specified is the weak form residual $\mathcal{R}^{\langle j\rangle}$ for the mechanical equilibrium Eq. (4). For the sake of simplicity, the mechanical problem is defined for the two-dimensional, rectangular design domain of Fig. 1. Under plane strain conditions, the 3D deformation gradient of the material at any point of the domain is defined as

$$\boldsymbol{F} = \boldsymbol{I} + \begin{bmatrix} \nabla\boldsymbol{u} & & 0 \\ & & 0 \\ 0 & 0 & 0 \end{bmatrix}. \tag{13}$$

A plane stress condition is not much more difficult to implement, but as demonstrated in [19], it constitutes a rather poor approximation of moderately thin hyperelastic structures with relatively complex geometry, compared to a 3D model.

A hyperelastic material is considered with a strain energy density function

$$\begin{aligned} \Psi = {} & \mathcal{E}(\chi)\left(\frac{K}{2}\ln^2|\boldsymbol{F}| + \frac{G}{2}\left(|\boldsymbol{F}|^{-2/3}\,\|\boldsymbol{F}\|^2 - 3\right)\right) \\ & + \frac{k_r}{2} K H^2\,\mathcal{I}(\chi)\mathbb{H}\boldsymbol{u} \vdots \mathbb{H}\boldsymbol{u}, \end{aligned} \tag{14}$$

where the first term is the common isotropic neo-Hookean material law from [20], with initial bulk modulus K and initial shear modulus G, weighted with the RAMP scaling from Eq. (3). The second term, involving higher order strains, is used for void regularization as suggested in [15], but in a somewhat simpler form. This term is scaled with a small dimensionless constant k_r, a dimensional scaling constant KH^2, and the void identity function $\mathcal{I}(\chi)$. The latter, is a smooth step function that transitions from 0 in non-void regions with $\chi > -5$, to 1 in void regions with $\chi < -6$. This smooth step transition function is adopted from [21] in the form

$$\mathcal{I}(\chi) = 6\left\langle -5-\chi\right\rangle^5_{[0,1]} - 15\left\langle -5-\chi\right\rangle^4_{[0,1]} + 10\left\langle -5-\chi\right\rangle^3_{[0,1]}. \tag{15}$$

Altogether, the hyperelastic strain energy Ψ from Eq. (14), with $\Psi \to \infty$ for $|\boldsymbol{F}| \to 0$, combined with a non-zero void contrast $\mathcal{E}_0$, ensures that the void can act as a third medium for contact between solid parts [15]. The void regularization term in Ψ, weighted with k_r, extends the applicability of the third medium contact model to rather large deformations and sliding. It should be reminded here, that this model has two limitations. It is only available for frictionless contact and intermediate density regions at the void solid interface are not fully compressed, resulting in a small gap between the contact surfaces, of size in the order of l_i.

The internal virtual work expression corresponding to the strain energy density function Ψ is

$$\begin{aligned} \Psi_{,\boldsymbol{u}}(\chi,\boldsymbol{u};\,\delta\boldsymbol{u}) = {} & \mathcal{E}(\chi)\overline{\boldsymbol{P}}(\nabla\boldsymbol{u}) : \nabla\delta\boldsymbol{u} \\ & + k_r\,KH^2\,\mathcal{I}(\chi)\mathbb{H}\boldsymbol{u} \vdots \mathbb{H}\delta\boldsymbol{u}, \end{aligned} \tag{16}$$

where $\overline{\boldsymbol{P}}$ is the in-plane 2×2 part of the 1st Piola–Kirchhoff stress tensor

$$\boldsymbol{P}(\nabla\boldsymbol{u}) = K\ln|\boldsymbol{F}|\,\boldsymbol{F}^{-\top} + G\,|\boldsymbol{F}|^{-2/3}\,\mathrm{dev}(\boldsymbol{F}\boldsymbol{F}^{\top})\boldsymbol{F}^{-\top}. \tag{17}$$

With the help of a scalar multiplier q and the Lagrangian

$$\int_{\Gamma_T} \frac{(u_y - d)\,q}{|\Gamma_T|}\,d\Gamma \tag{18}$$

an average vertical displacement d can be imposed on the top side of the domain, Γ_T, simply by seeking the stationary point of the Lagrangian. The scaling of the integrand with $1/|\Gamma_T|$ is required because of the definition of the scalar multiplier q in units of force.

In total, combining the virtual work Eq. (16) and the contributions of the Lagrangian from Eq. (18) for a specific displacement $d^{\langle j\rangle}$, yields the weak form for mechanical equilibrium at the corresponding control point j as

$$\begin{aligned} \mathcal{R}^{\langle j\rangle}(\chi,\boldsymbol{u},q\,;\delta\boldsymbol{u},\delta q) = {} & T\cdot\int_\Omega \Psi_{,\boldsymbol{u}}(\chi,\boldsymbol{u}\,;\delta\boldsymbol{u})\;d\Omega \\ & - \int_{\Gamma_T} \frac{q\,\delta u_y + \left(u_y - d^{\langle j\rangle}\right)\delta q}{|\Gamma_T|}\;d\Gamma. \end{aligned} \tag{19}$$

Additional displacement constraints can be imposed by restricting the solution space for $\boldsymbol{u}$ accordingly, i.e. by eliminating degrees of freedom or by reducing degrees of freedom through slave-master relationships. For the model shown in Fig. 1 for example, all horizontal degrees of freedom on the left side Γ_L are reduced to a single degree of freedom u_{Lx}. In order to avoid horizontal rigid body motion, all horizontal degrees of freedom on Γ_R are substituted with $-u_{Lx}$. All vertical degrees of freedom on Γ_B are removed and all vertical degrees of freedom on Γ_T are reduced to a single master degree of freedom u_{Ty}. Moreover, periodicity conditions are imposed by interlinking all horizontal degrees of freedom on Γ_T with the corresponding ones on Γ_B, as well as all vertical degrees of freedom on Γ_R with the corresponding ones on Γ_L.

With the definition of the weak form $\mathcal{R}^{\langle j\rangle}$ in Eq. (19), the problem definition is completed and the system of Eqs. (4), (7) and (8) can be solved. During the pseudo-time integration towards $t = \infty$, this system is solved repeatedly, where the only changes from step to step is an update of the previous design field χ^*, and a possible adaptation of the time step Δt.

2.6. Robust formulation

In few of the numerical examples shown later, the optimization process can exploit the nonlinear behavior of severely deformed intermediate density material for achieving the requested nonlinear response. This can result in non discrete designs despite the volume penalization in Eq. (11). For this reason, in order to enforce discrete black and white solutions, robust topology optimization, according to [22,23], is used for some of the numerical examples.

For the design parametrization described in Section 2.2, it is easy to realize eroded and dilated designs by applying a constant offset to the design variable field χ. On a fully established interface between solid and void, the slope of the design field χ is equal to $8/l_i$, cf. Eq. (12). Offsetting the field χ by a constant η results in a uniform dilation of the solid-void interface by a distance equal to $l_i\cdot\eta/8$. A negative offset η will lead to a corresponding erosion of the design.

In regions of intermediate density material however, where no clear void-solid interface is established, adding a positive offset η to the design field will shift the entire region very much towards solid, while the opposite will occur for a negative offset. This effect can be utilized when the aim is to prevent the exploitation of nonphysical intermediate density material. Including some performance measure for the dilated or eroded design in the objective function is an effective method for preventing such non nonphysical solutions. For a graphical illustration of how a design field offset affects the density and stiffness distributions, the reader is referred to Fig. 15 in Appendix A.

In the present work, for objectives requiring a softening spring response under tension, a dilated design realization is included in the objective function. The objective function C, cf. Eq. (1), contains a contribution $C_q^{\langle j_d\rangle}$ from a control point with index j_d, which corresponds to the dilated design. This design is subjected to a prescribed displacement $d^{\langle j_d\rangle}$, with $q^{\langle j_d\rangle}$ being the actual reaction force, and $q_*^{\langle j_d\rangle}$ the target reaction force. The only modification in the model equations, for this specific control point j_d, is that χ in all occurrences of the mechanical residual $\mathcal{R}^{\langle j_d\rangle}$ is substituted with $\chi+\eta_d$, with η_d being the dilation offset value.

2.7. Implementation

The system of Eqs. (4), (7) and (8) has been implemented using the general weak form language and the C++ API of the GetFEM library [24], within a single monolithic model object. The linearization of the provided equations and the assembly of the resulting tangent system is performed automatically by the framework described in [24].

For the discretization of the equations, a structured mesh has been used, corresponding to a Cartesian $N \times N$ grid over the domain Ω. Numerical integration is performed in all cases with nine Gauss points per quadrilateral element. Quadrilateral 9-node Lagrange elements are used for the solution spaces of all displacement fields $\boldsymbol{u}^{\langle j\rangle}$ and the respective test functions $\delta\boldsymbol{u}^{\langle j\rangle}$. These finite element spaces are further reduced according to the boundary conditions described in Section 2.5. Being already scalars, the unknowns $q^{\langle j\rangle}$ and corresponding variations $\delta q^{\langle j\rangle}$ require no discretization.

A smooth C^1-continuous solution space is used for the discretization of the design field χ, as well as the respective test functions $\delta\chi$, in order to provide a consistent representation of the higher order derivatives appearing in the regularization term in Eq. (12). In particular, quadratic B-spline basis functions are used for χ, defined in the same Cartesian grid as the Lagrange finite elements for the displacements. In total, apart from special B-spline basis functions at the borders, there is one degree of freedom for χ per element, and it is reminded that the density ρ is always bounded between 0 and 1, as per definition, cf. Eq. (2). Due to its higher regularity, the B-spline discretization of χ, introduced here, is a superior option compared to the linear elements used previously in [15]. No boundary conditions are imposed to the design field χ on the left and right boundaries, Γ_L and Γ_R, respectively. Mirror symmetry conditions are imposed on the bottom and top side, Γ_B and Γ_T, simply by removing all basis functions with non-zero gradients in a direction normal to the respective boundary. In addition, a major reduction in the solution space of χ is performed for imposing mirror symmetry with respect to the horizontal and vertical axes through the center of the rectangular domain Ω, cf. Fig. 2. All degrees of freedom in the SE, NE, and NW quadrants of the domain are coupled to the corresponding independent degrees of freedom in the SW quadrant. It is reminded that this symmetry constraint applies only to the design variable χ. The displacement field $\boldsymbol{u}$ is defined in the entire domain, without imposing any symmetry constraint to the solution.

The assembly of the linearized and discretized system results in a monolithic linear system of equations that forms the core of a Newton–Raphson loop for performing a design update from χ^* to χ. Upon convergence of the Newton–Raphson loop, the stored previous design χ^* is updated and the optimization can proceed with the next pseudo-time step. The number of Newton–Raphson iterations required for convergence is a very useful and meaningful measure of non-linearity in the model. For a very small time step Δt, the Newton–Raphson loop will converge within very few iterations, indicating that larger time steps may be performed. Using this heuristic, Δt is adjusted adaptively during the optimization procedure. If a time step is solved using less than six Newton–Raphson iterations, Δt is increased by a factor of two for the next step, while it is reduced by a factor of four, if the current step fails to converge, and the step is repeated. The optimization is completed when the time step Δt has grown to a level that allows for the coupled system of optimality, adjoint and mechanical equilibrium equations to be solved by Newton–Raphson, without any damping with respect to χ.

3. Numerical results and discussion

A topology optimization model has been introduced for the inverse design of nonlinear springs with a pointwise prescribed load–displacement response. In this section, optimization results are presented for concrete examples with specific input parameters, initial design and for different target responses. Moreover, numerical results are shown from an extension of the plane strain model to the axisymmetric case.

Fig. 2 shows the density distribution $\rho(\chi)$ of the initial guess that all optimizations start with, and Table 1 provides all relevant model parameters, used in the numerical examples, unless otherwise stated in the text. The length of the mechanical spring is equal to the domain height H and control points are considered at fixed end-point displacements of 10% and 20% of the spring length, either in compression or tension, i.e. $d^{\langle j\rangle}/H = \pm 0.1$ and $d^{\langle j\rangle}/H = \pm 0.2$.

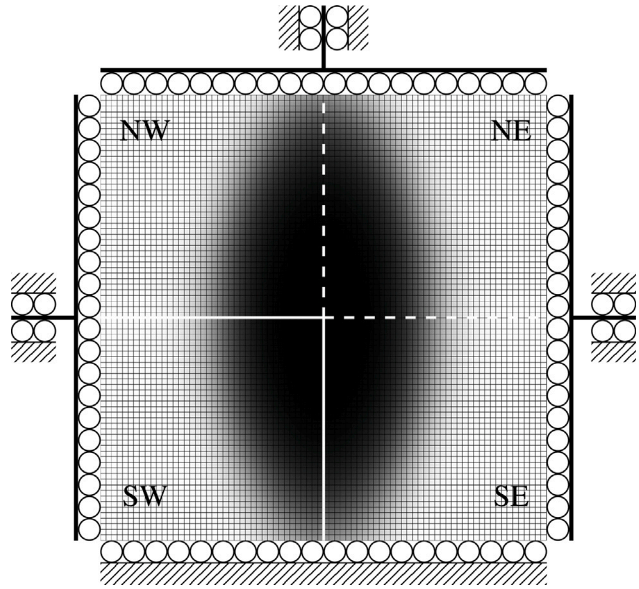

Fig. 2. Initial density distribution. The design is constrained to be symmetric about both the x- and y-axis, as illustrated in the figure.

Table 1
Default model parameters for all examples unless otherwise specified in text.

Domain dimensions	$L \times H$	100×100	mm^2
Out-of-plane thickness	T	1	mm
Mesh size		80×80	–
Solid bulk modulus	K	5/3	MPa
Solid shear modulus	G	5/14	MPa
Void/solid stiffness contrast	$\mathcal{E}_0$	10^{-6}	–
Void regularization scaling	k_r	10^{-6}	–
Control point weights	$w_q^{\langle j\rangle}$	1	N^{-2}
Volume minimization weight	k_ρ	10^{-8}	–
Minimum interface width	l_i	1	mm
Interf. width p-norm exponent	n	6	–
Interf. width p-norm weight	k_i	10^{-2}	–
Level-set regularization weight	k_H	10^{-9}	–
Transient length scale	l_t	8	mm

Before showing specific numerical examples, it is useful to explain the optimization convergence for just one representative case. Fig. 3 shows the convergence history for one of the cases that will be shown later, where a spring is topologically optimized for achieving a linear response between 10% elongation and 20% compression. The uppermost diagram shows the pseudo-time step Δt as a function of the design iterations in a logarithmic scale. After approximately 85 design iterations, the time-step increases monotonically until it reaches the limit of 10^{20} after 115 design updates. Then, the history dependent term in Eq. (12) is removed and a final step is performed to solve for the exact optimality point.

The monolithic solution of physics, optimality and adjoint equations, just with a damping of the design variable, as described in Section 2, leads to a monotonically decreasing objective function C over the entire optimization history as shown in the second diagram in Fig. 3. Unlike staggered schemes, there are no oscillations in any phase of the optimization. It is reminded that according to Eq. (1), C includes the actual optimization objective contributions $C_q^{\langle j\rangle}$ with regard to the target response at all control points j, as well as volume penalization, design constraints and regularization included in the functional C_χ.

The third diagram in Fig. 3 shows the individual contributions of the three control points considered in this example. After less than 20 design iterations, all three values become practically zero, indicating

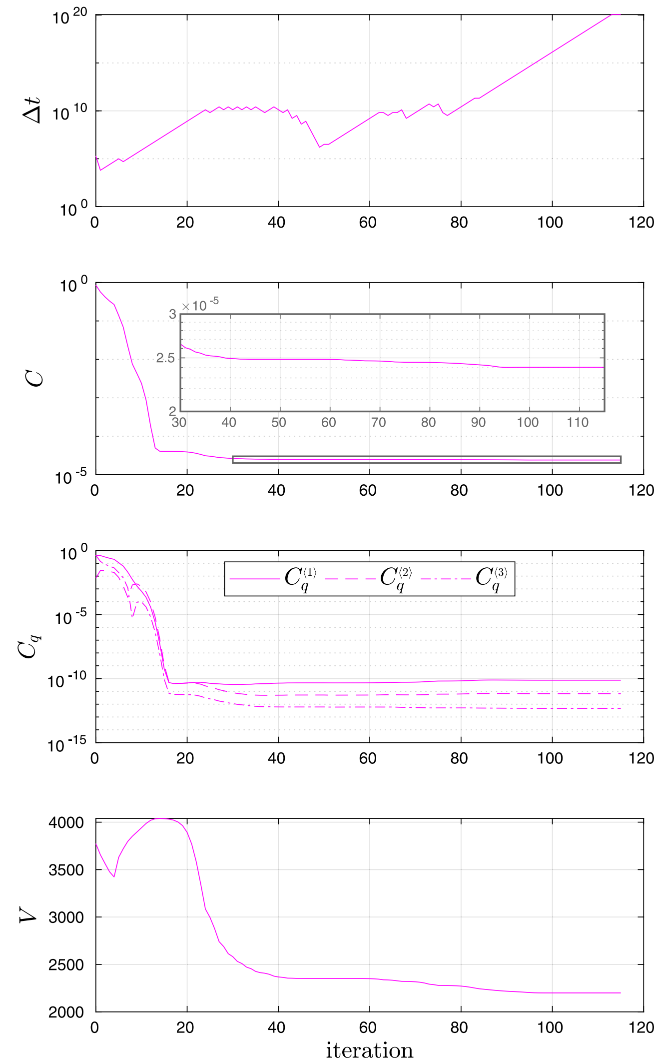

Fig. 3. Representative design iteration history, for the inverse design of spring C4 with linear response under compression (cf. Fig. 4 and middle row in Fig. 5). The plotted value for C in the second diagram is evaluated for $\dot{\chi} = 0$.

that the target response has been reached with insignificant deviations. The last diagram in the figure shows the evolution of the design volume V according to Eq. (10). It turns out that after the 40th design iteration, the volume penalization term dominates the objective. For this reason, in the last phase of the optimization the total volume of utilized material decreases towards its final value, with all designs during this phase still fulfilling the target response.

3.1. Compression springs

A contact-aware optimization appears to be especially suited for designing structures in compression, where internal collisions are more likely. Moreover, internal contact can be exploited as a nonlinear effect for achieving a desired response when designing a spring loaded in compression.

For this reason, as a first example, a series of springs have been designed, which exhibit either stiffening or softening behavior under compression. Fig. 4 shows the target control points along with the resulting load–displacement responses of the optimized designs. Two control points for 10% and 20% compression are used for prescribing the desired, in general nonlinear, response under compression, and one additional control point for 10% tension is used in order to ensure

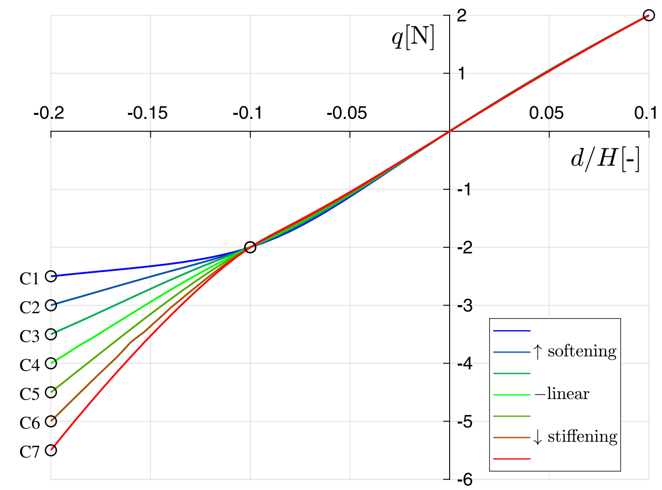

Fig. 4. Target control points (circular markers) and resulting load–displacement curves for the optimized compression spring designs shown in Fig. 5.

Table 2
Target reaction forces at control points with $d^{(1)} = 0.1H$, $d^{(2)} = -0.1H$, and $d^{(3)} = -0.2H$, for all 7 optimized compression springs.

Case	C1	C2	C3	C4	C5	C6	C7	
$q_*^{(1)}$		…		2		…		N
$q_*^{(2)}$		…		−2		…		N
$q_*^{(3)}$	−2.5	−3	−3.5	−4	−4.5	−5	−5.5	N

connectivity in the design. The exact values for all target control points are provided in Table 2.

All seven fully converged designs are shown in Fig. 5 in their undeformed state, as well as in deformed states corresponding to the three control points used for the optimization. All set target points are met remarkably well. In the range between ±10% end-point displacement, all designs follow a relatively linear load–displacement relation, as dictated by the first two control points. Beyond the first control point in compression, the curves transition smoothly to an either stiffer or more compliant response in order to match the required target value at the ultimate control point.

All solutions have the same topology, in the form of a single column with a hole located at its center, but the shape of the hole varies significantly. All designs combine two distinct nonlinear mechanisms in order to achieve the requested response. The first mechanism consists in a progressive outwards buckling of the walls of the internal hole, which leads to a reduction in the tangent stiffness of the overall column. The second effect contributing to the overall nonlinear response of the structure is the onset of contact between different portion of the internal hole walls. Although the onset of contact always has a stiffening effect it is also present in designs that target an overall softening response. This is to counteract any excessive loss of stiffness due to the first mechanism. In total, the results from Fig. 5 clearly demonstrate how the modeling of contact is essential for optimizing structures with a desired mechanical response under compression. Maybe apart from the very first case with the strongest softening behavior, none of the remaining designs could have been obtained without accounting for internal contact.

Fig. 5 also reports the total material volume for each of the designs. However, instead of reporting the actual material volume directly, a dimensionless quantity is reported which is easier to interpret. Assuming that the available material is redistributed to form a straight column of width $\overline{W}$ and height H, while preserving the given material volume V, the following relation holds

$$\overline{W} = \frac{V}{HT}. \tag{20}$$

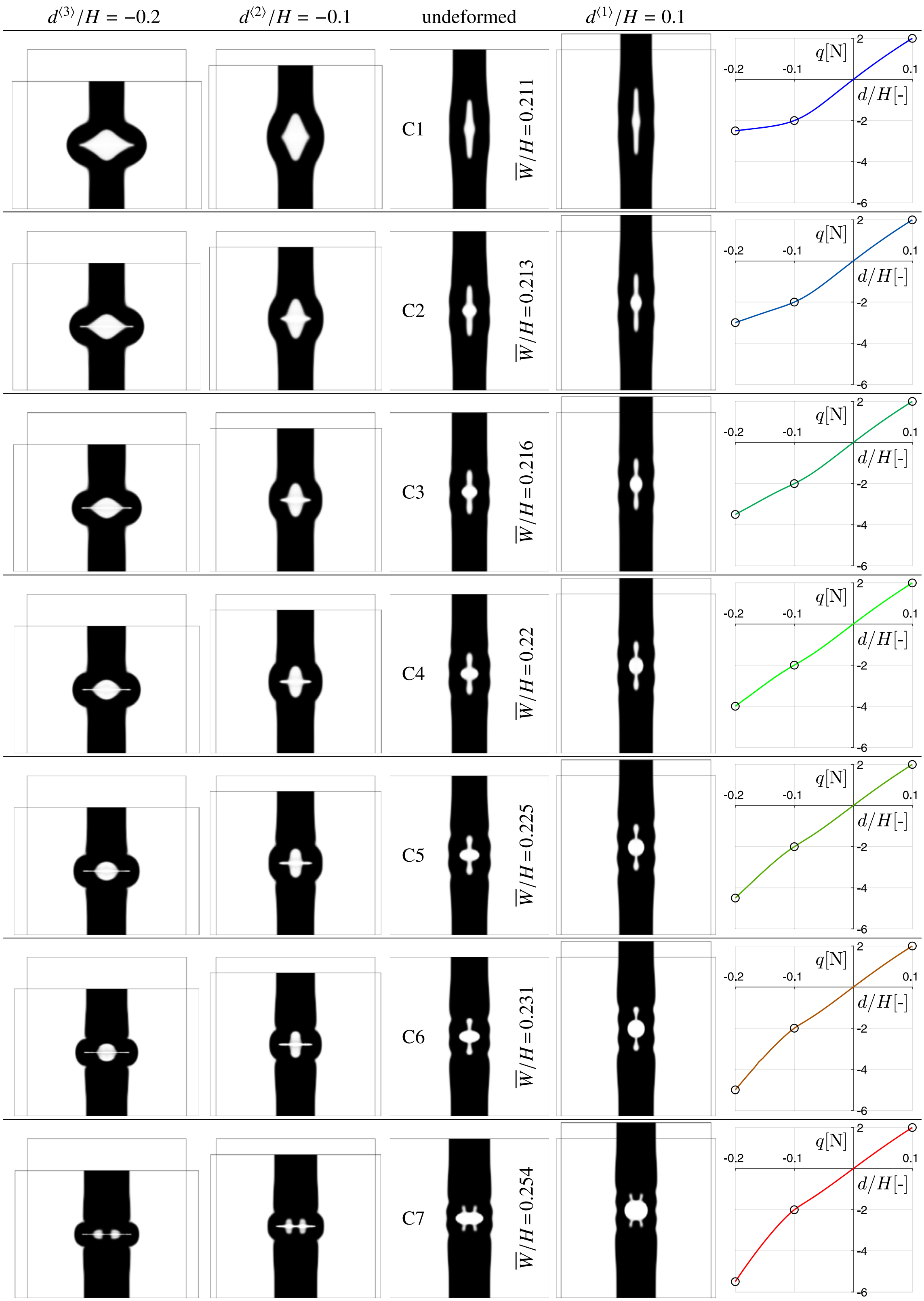

Fig. 5. Compression spring designs optimized for the response shown in the last column.

Table 3
Target reaction forces at control points with $d^{(1)} = 0.1H$ and $d^{(2)} = 0.2H$, for all 6 optimized tension springs.

Case	T1	T2	T3	T4	T5	T6	
$q_*^{(1)}$	⋯		2		⋯		N
$q_*^{(2)}$	3	3.5	4	4.5	5	5.5	N

The aspect ratio $\overline{W}/H$ of the volume-equivalent straight column is reported in Fig. 5 instead of V. It is seen that the higher the stiffening requirement imposed by the third control point in the objective, the larger the material usage.

It is possible that some of the target responses could also be achieved without relying on internal contact. However, it is unlikely that such solutions would be as material efficient as the ones reported in Fig. 5, which deliberately exploit contact for achieving the desired objective. Designs not involving contact are in fact contained in the optimization space of the present model, and can actually be reached unless another local minimum is found first. The fact that only one solution not involving contact was found (C1), is a strong indication that leveraging contact is really advantageous in all other cases under compression. In addition, if the same optimization would be repeated without modeling internal contact, all resulting designs should be carefully examined for potential overlaps upon deformation that may render the solution physically meaningless.

As is the case in most topology optimization problems, the choice of the initial design will have an impact on which local minimum the optimization will eventually reach. All cases presented in this section start with the initial design from Fig. 2 which resembles a column. For an indication on how the model performs with a less structured initial design, the reader is referred to Appendix B, where an alternative optimization of case C7 is presented, starting with a randomized grayscale distribution instead of the regular initial design.

3.2. Tension springs

Although internal contact is more relevant for springs under compression, it is still very interesting to demonstrate how the proposed method performs when applied to springs under tension. For this purpose, six target responses are considered, described by two control points at 10% and 20% tension. Fig. 6 shows all target control points and the actual load–displacement curves for the designs obtained for the different targets. The exact coordinates of all control points are provided in Table 3.

As it was the case for compression springs, all target points are satisfied remarkably well. There is however, a big difference between designs that are optimized for a softening response compared to designs optimized for a linear or stiffening load–displacement curve. A major challenge for designing springs with a softening response in tension is that the optimization procedure will in general exploit the low stiffness of intermediate density material in order to create a zone with strongly localized deformations that leads to the desired response, but with a design that is not physical. Such solutions are shown in Fig. 14 in Appendix A. In order to suppress this possibility, the robust formulation from Section 2.6 is employed, and an extra control point is added at 20% tension for a design which is dilated with 0.25 mm, compared to the blueprint design. The offset η_d of the design field χ, for achieving this dilation is found from the condition

$$\eta_d \cdot l_i / 8 = 0.25\,\mathrm{mm}.$$

This is a new length scale introduced to the model, in addition to the interface width l_i. It has to be chosen according to the absolute size of the small features that need to be controlled. For example the neck in the undeformed design T1 has a width of approximately 4 mm in the blueprint version, which then increases to 4.5 mm in the dilated version of the design.

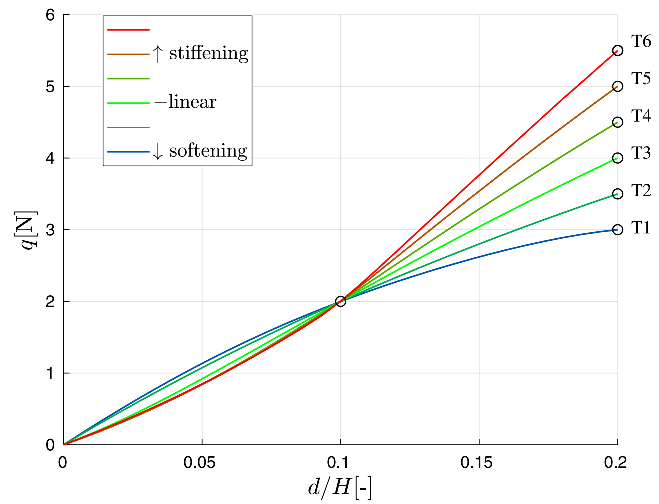

Fig. 6. Target control points (circular markers) and resulting load–displacement curves for the optimized tension spring designs shown in Fig. 7.

The extra control point for the dilated design, at $j_d = 3$, is the same as the second control point, i.e. $d^{\langle 3 \rangle} = d^{\langle 2 \rangle}$ and $q_*^{\langle 3 \rangle} = q_*^{\langle 2 \rangle}$. The weight for this control point, $w_q^{\langle 3 \rangle} = 10^{-4}\,\mathrm{N}^{-2}$, is much smaller than the standard weight for all other control points, cf. Table 1. Nevertheless, it is sufficient for providing the discrete designs shown in the first two rows in Fig. 7, instead of the respective grayscale designs provided in Fig. 14 in Appendix A. Apart from including a dilated version of the design to the objective, for these two cases, it is also necessary to use a finer 160×160 mesh, instead of the standard 80×80 mesh. The finer mesh allows to better resolve the narrow neck formed at the top and bottom of the design.

The two cases with a softening load–displacement response, exploit strain localization in a very narrow neck in order to achieve the desired target. Although these designs are not practical, due to excessive strains, they demonstrate an interesting and new result. To the authors best knowledge, there are no prior large strain topology optimization models that deliberately exploit necking in order to achieve a target softening response in tension.

More practical are the designs obtained for a linear or stiffening response under tension, shown in the last four rows in Fig. 7. All of them utilize a well-known mechanism in which initially curved and therefore more compliant members gradually straighten upon loading, thereby increasing the overall stiffness of the structure. Interestingly, in addition to this established mechanism, the optimization procedure for the last three cases also leverages internal contact to achieve the desired stiffening response.

Material usage is also reported in Fig. 7, again in terms of the volume-equivalent straight column aspect ratio $\overline{W}/H$. As expected, more material is required for designs that target a stronger stiffening response. The only exception is the first design, which targets a strong softening response, and it nevertheless utilizes a rather large volume of material in order to form the neck where strain localization occurs.

3.3. Combined compression and tension springs

The next step is to try to design springs with tailored response in both compression and tension. Due to the particularities of the designs obtained for softening in tension, only linear and stiffening responses are requested for the tension side. These are then combined with different target responses in compression, which range from softening to stiffening. Springs have been designed for a series of target responses between −20% and +20% end-point displacement, described by means

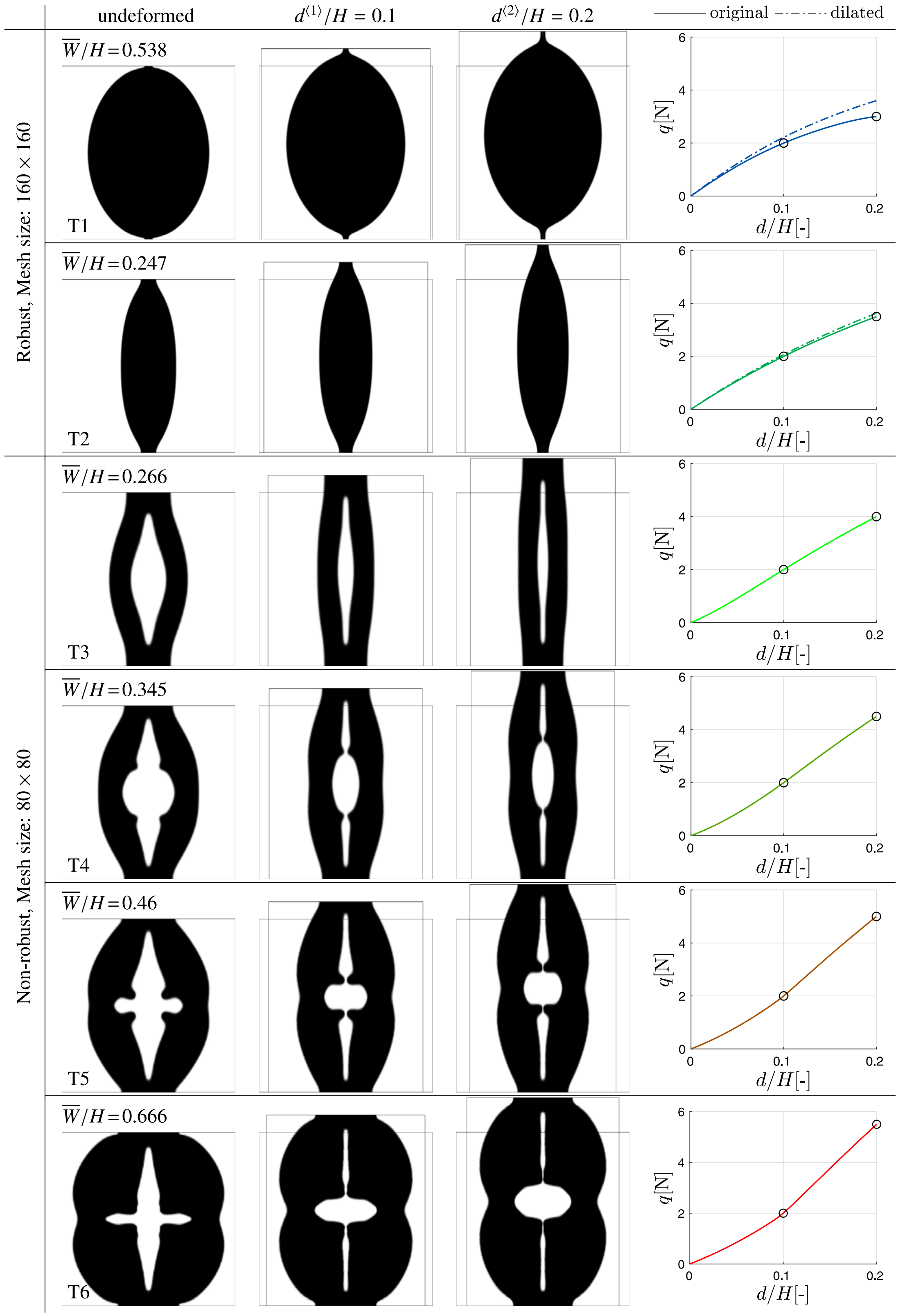

Fig. 7. Tension spring designs optimized for the response shown in the last column.

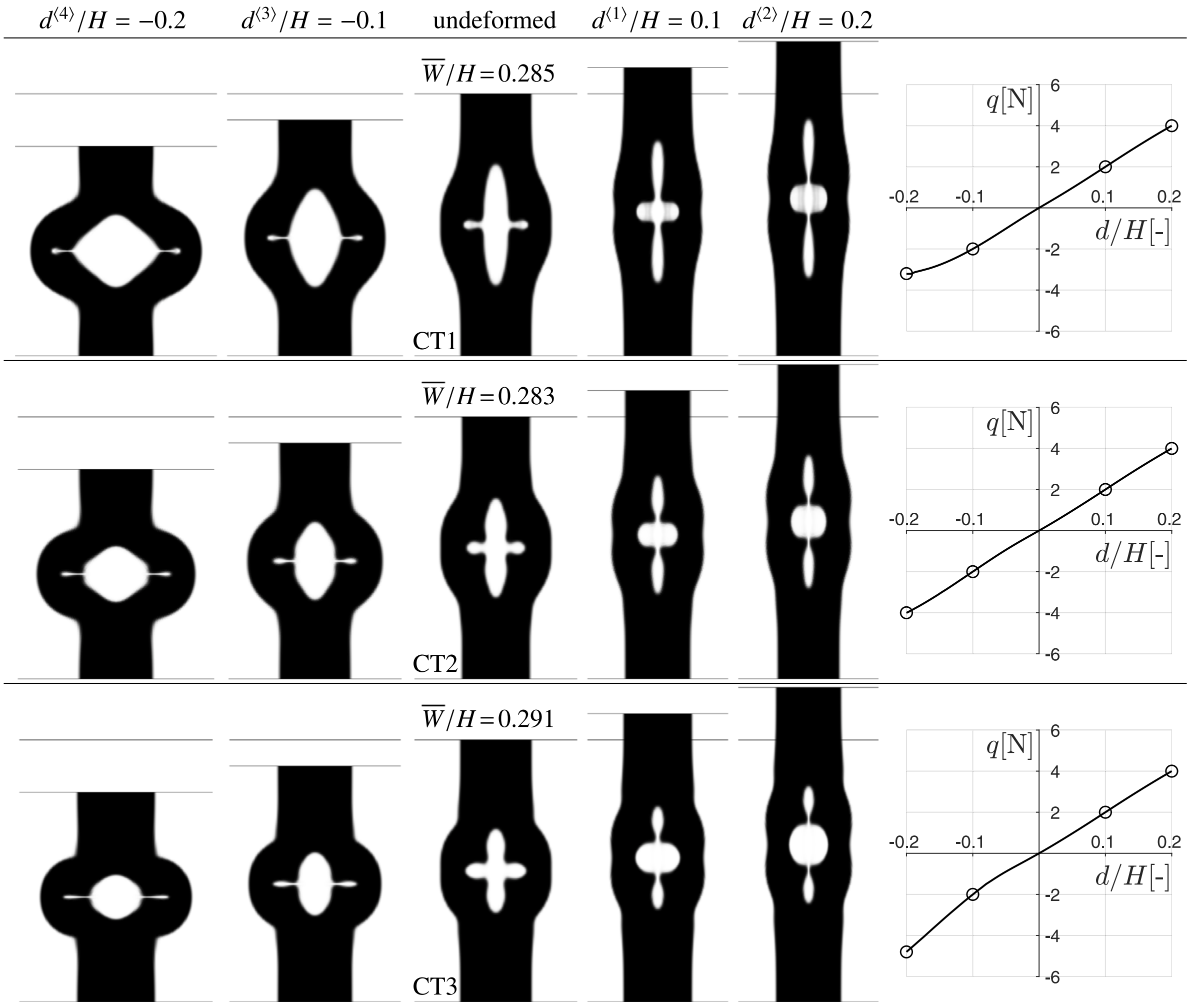

Fig. 8. Tension–compression spring designs optimized for the response shown in the last column.

Table 4
Target reaction forces at control points with $d^{\langle 1\rangle} = 0.1H$, $d^{\langle 2\rangle} = 0.2H$, $d^{\langle 3\rangle} = -0.1H$ and $d^{\langle 4\rangle} = -0.2H$ for all 6 optimized compression–tension springs.

Case	CT1	CT2	CT3	CT4	CT5	CT6	
$q_*^{(1)}$	…		2		…		N
$q_*^{(2)}$	4	4	4	4.8	4.8	4.8	N
$q_*^{(3)}$	…		−2		…		N
$q_*^{(4)}$	−3.2	−4	−4.8	−3.2	−4	−4.8	N

of four control points, two on the compression side and two on the tension side.

Fig. 8 shows results obtained for a linear response in tension and softening, linear, or stiffening response in compression. Fig. 9, shows the respective designs obtained for a moderate stiffening response in tension. All control points for the six cases from these two figures are defined in Table 4.

3.4. Axisymmetric springs

After having demonstrated how the proposed method performs for designing springs under plane strain conditions, an extension to axisymmetric springs is rather simple. A vertical symmetry axis is considered through the center of the domain Ω shown in Fig. 1. Only half of the domain for $x > 0$ is considered, denoted Ω^+, and the coordinate x is renamed to r.

The mechanical model for the axisymmetric structure is obtained simply by an appropriate redefinition of the 3D deformation gradient as

$$\boldsymbol{F} = \boldsymbol{I} + \begin{bmatrix} \nabla\boldsymbol{u} & & 0 \\ & & 0 \\ 0 & 0 & u_r/r \end{bmatrix}, \tag{21}$$

instead of the plane strain definition from Eq. (13). In this definition, u_r is the radial (i.e. horizontal) component of the displacements field.

This change affects the virtual work expression from Eq. (16), which becomes

$$\begin{aligned}\Psi_{,\boldsymbol{u}}(\chi, \boldsymbol{u};\, \delta\boldsymbol{u}) = \mathcal{E}(\chi)\left(\overline{\boldsymbol{P}}(\nabla\boldsymbol{u}) : \nabla\delta\boldsymbol{u} + P_{33}/r\,\delta u_r\right) \\ + k_r\,K H^2\,\mathcal{I}(\chi)\mathbb{H}\boldsymbol{u} \vdots \mathbb{H}\delta\boldsymbol{u},\end{aligned} \tag{22}$$

where P_{33} is the out-of-plane normal stress component of the 1st Piola–Kirchhoff stress tensor $\boldsymbol{P}$.

Apart from the new definition of $\boldsymbol{F}$, all volume integrals of the form $T \cdot \int_{\Omega} \ldots d\Omega$ need also to be replaced with integrals in the form $\int_{\Omega^+} 2\pi r \ldots d\Omega$. For instance, the material volume for the axisymmetric design is computed as

$$V = \int_{\Omega^+} 2\pi\, r\, \rho(\chi)\; d\Omega. \tag{23}$$

and the weak form Eq. (19) for mechanical equilibrium is replaced by

$$\begin{aligned}\mathcal{R}^{\langle j\rangle}(\chi, \boldsymbol{u}, q\,; \delta\boldsymbol{u}, \delta q) = \int_{\Omega^+} 2\pi r\,\Psi_{,\boldsymbol{u}}(\chi, \boldsymbol{u}\,; \delta\boldsymbol{u})\;\, d\Omega \\ - \int_{\Gamma_T^+} 2\pi r \frac{q\,\delta u_y + \left(u_y - d^{\langle j\rangle}\right)\delta q}{\pi\left|\Gamma_T^+\right|^2}\;\; d\Gamma.\end{aligned} \tag{24}$$

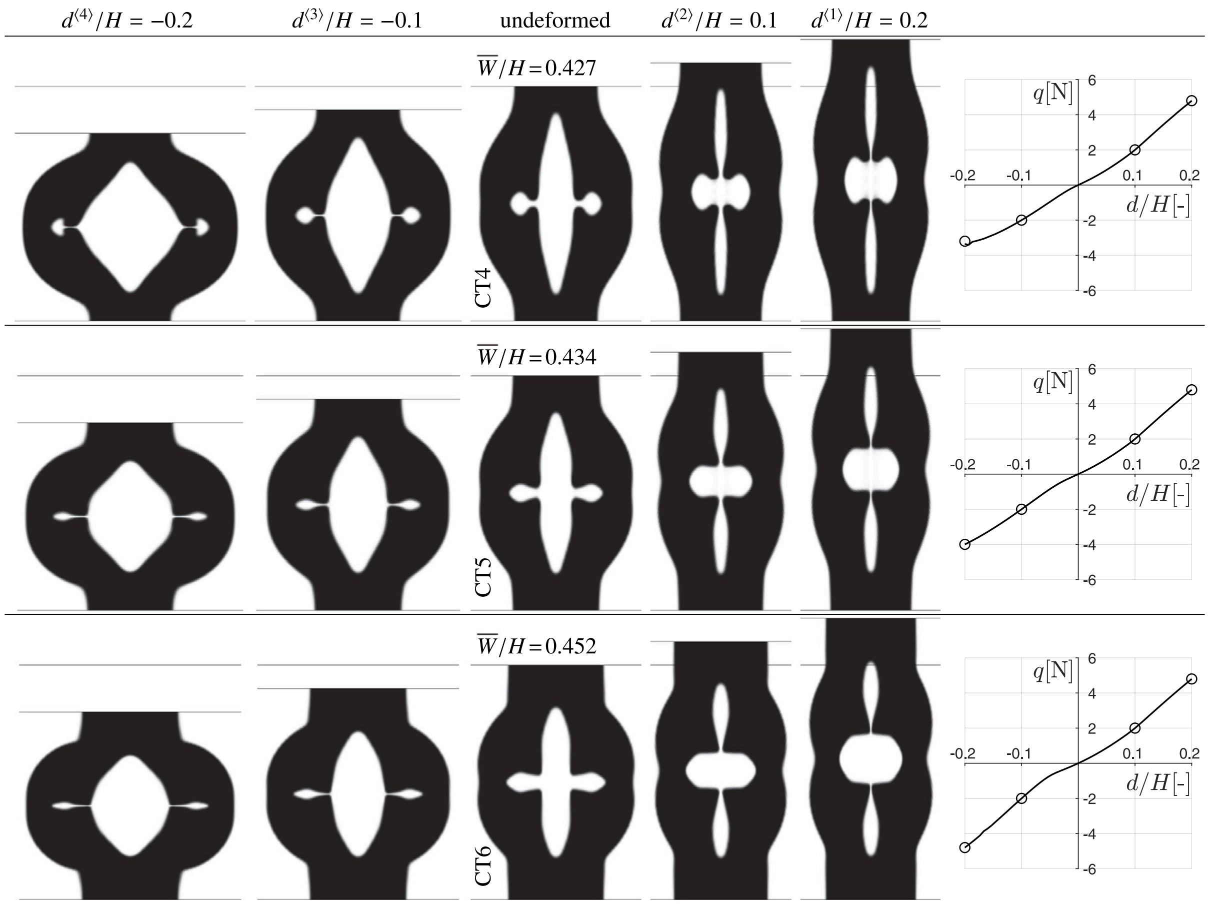

Fig. 9. Tension-compression spring designs optimized for the response shown in the last column.

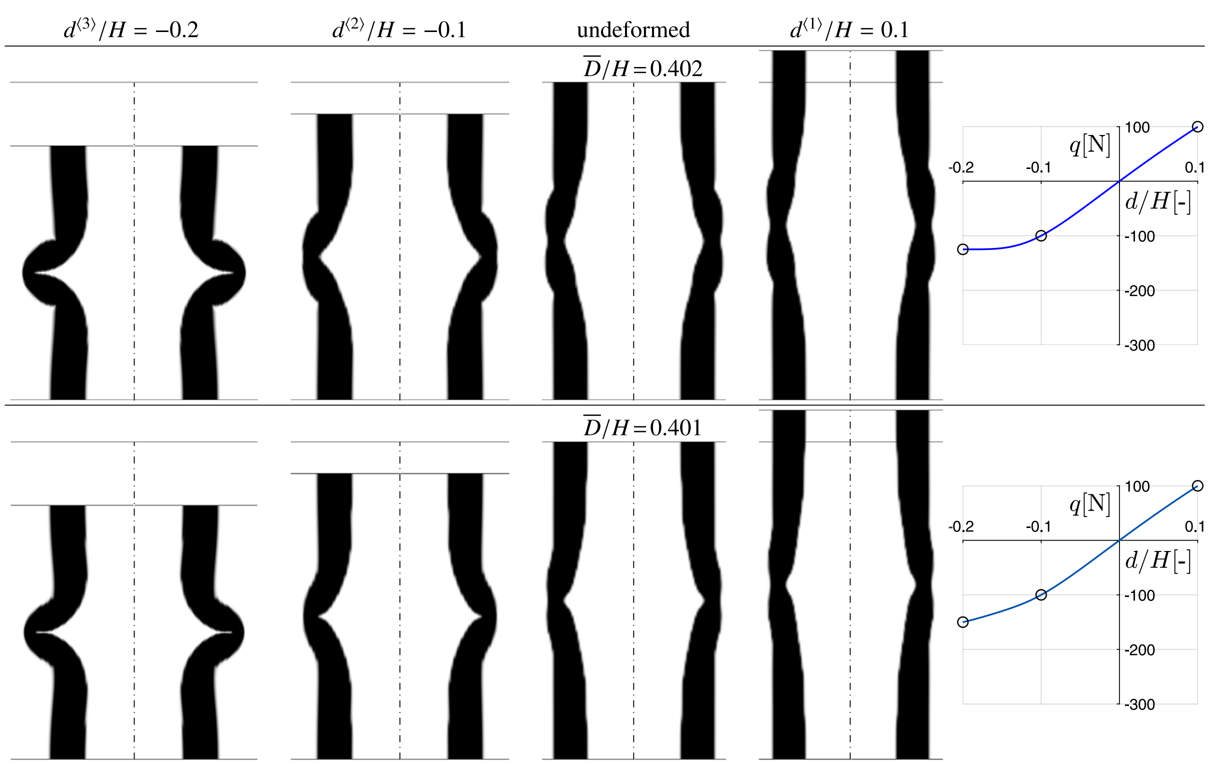

Fig. 10. Axisymmetric compression spring designs optimized for the softening response shown in the last column.

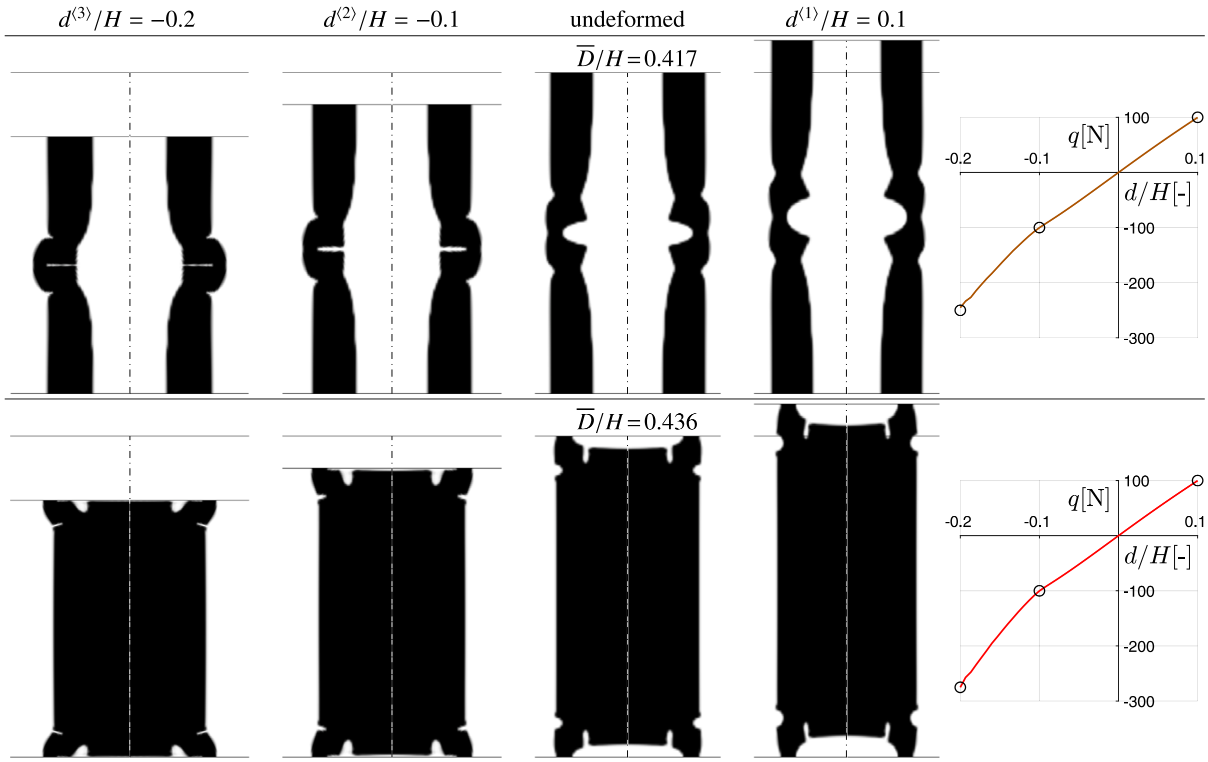

Fig. 11. Axisymmetric compression spring designs optimized for the stiffening response shown in the last column.

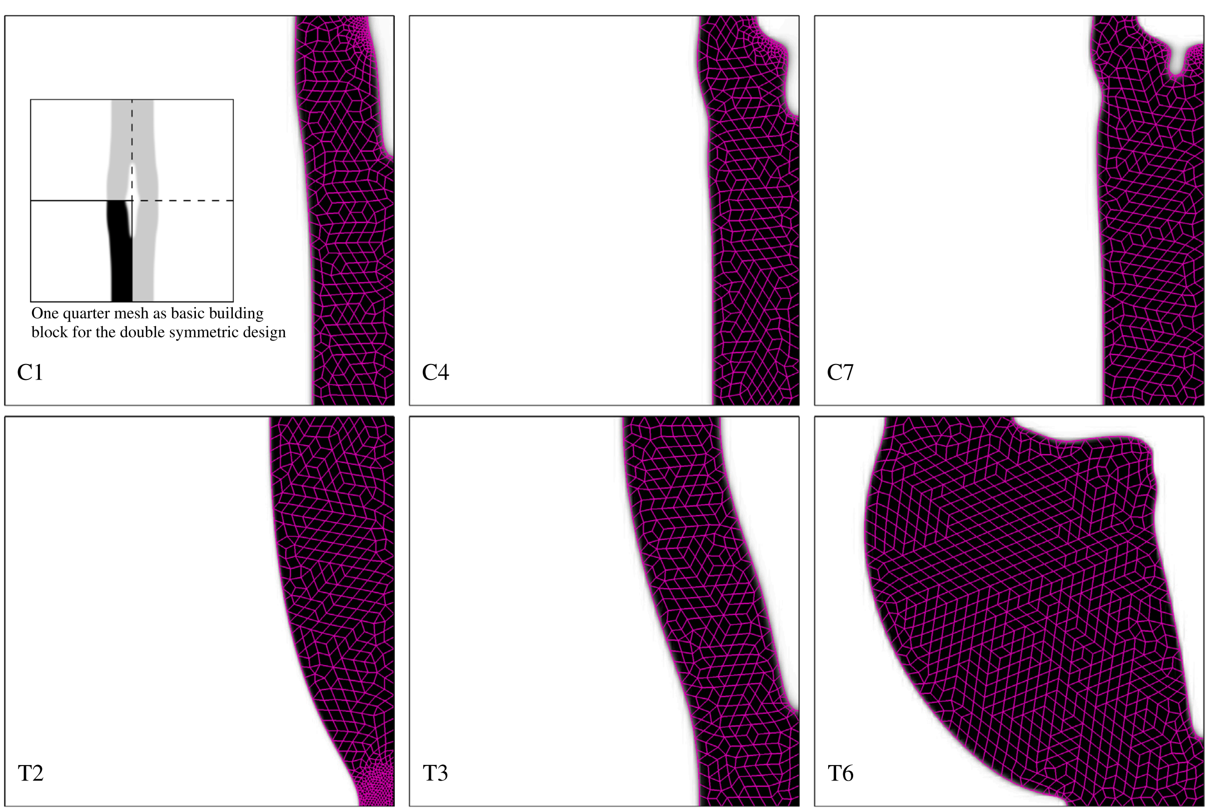

Fig. 12. Lower left quarter of the body fitted meshes used for post-evaluation of selected designs.

With these rather minor modifications on top of the plane strain model, the axisymmetric designs shown in Figs. 10 and 11 could be obtained, respectively, for two softening and two stiffening target responses, under compression. The first three designs possess the topology of a hollow tube and the outward buckling of the walls is again combined with internal contact in order to achieve the target responses,

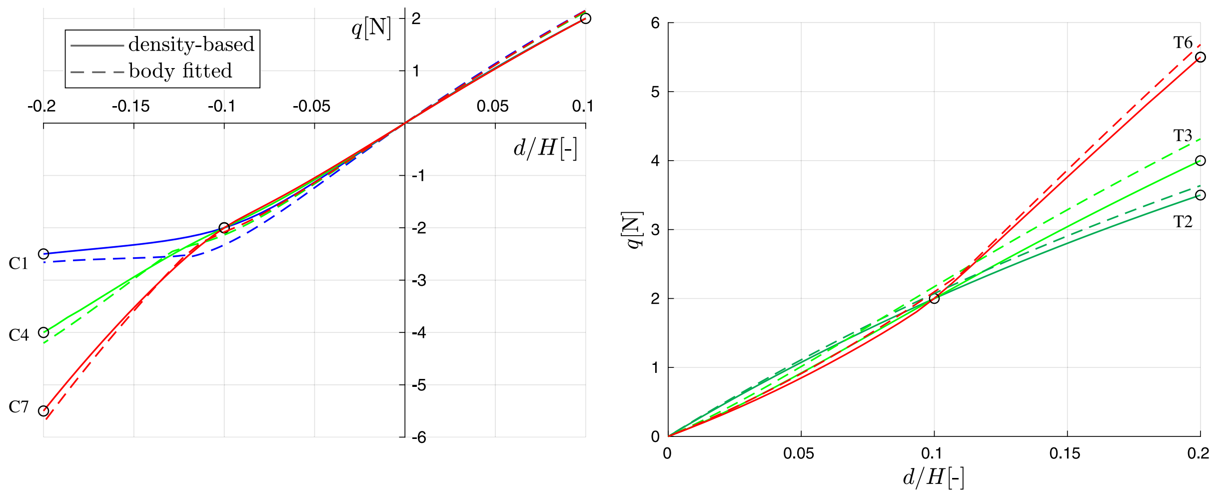

(a) Compression springs (b) Tension springs

Fig. 13. Comparison of load–displacement curves for a selection of density-based optimized designs (solid lines) and corresponding post evaluation curves based on body fitted meshes (dashed lines).

as was the case for the plane strain model. The same mechanisms are present also in the last case shown in Fig. 11, which has the topology of an axisymmetric column with an embedded hole split between the bottom and the top of the domain. This is the equivalent of the last plane strain case from Fig. 5.

Figs. 10 and 11 report also utilized material volume for each design. This is now given for the axisymmetric geometries in terms of the volume-equivalent solid cylinder aspect ratio $\overline{D}/H$, where

$$\overline{D} = \sqrt{\frac{4V}{\pi H}} \tag{25}$$

is the diameter of a solid cylinder with height H that occupies the same volume V as the respective axisymmetric design.

3.5. Post-evaluation

All results shown so far consist of satisfactorily discrete designs which contain grayscale material only in a refined zone of width $l_i = 1$ mm at the interface between solid and void, corresponding to ca. 4/5 of an element size. Although the intermediate density zone at the solid-void interface is in the order of only 1/100 of the domain size, it can still introduce inaccuracies with respect to the actual mechanical response of a fully discrete design. The only reliable manner of evaluating such inaccuracies is by remodeling the obtained designs, using sufficiently fine body fitted meshes and conventional contact modeling.

A total of six cases were selected for reevaluation, among the plane strain designs provided in Sections 3.1 and 3.2. The criterion for this selection was the presence of fine features, where intermediate density material is expected to have the most detrimental effect on the accuracy of the model. Fig. 12 shows body fitted meshes for the lower left quarter of each of the six designs. Due to the imposed symmetry in the designs, such body fitted meshes were initially created for only one quarter of each design, using GMSH [25] at a threshold value $\chi = 0$, i.e. $\rho = 0.5$. The generated meshes, seen in Fig. 12, were then mirrored with respect to both the horizontal and vertical axes in order to obtain the mesh for the entire model used in the post-evaluation. For the post-evaluation, second order elements were used, with six nodes per triangle and nine nodes per quad element. The same boundary conditions were applied to the top and the bottom sides of the body fitted meshes, as shown in Fig. 1 for the topology optimization model. Frictionless contact for the internal walls of the structure was modeled using the augmented Lagrangian formulation from [26] with quadratic approximation of the contact multiplier and seven Gauss points per element side.

Load–displacement curves obtained from the post-evaluation of all six cases are plotted over the respective original load–displacement curves in Fig. 13. The deviations between the response accounted for during the optimization and the actual response obtained through the post-evaluation are visible but rather limited. For the two compression springs with linear (C4) and stiffening (C7) response, seen in Fig. 13a, the inaccuracies due to the density-based approximation of the solid are insignificant. The largest deviation is observed for the compression spring optimized for a softening response (C1), but still the post-evaluation response exhibits just slightly stronger softening behavior than the optimization target. For the three tension springs (T2,T3,T6) post-evaluation, seen in Fig. 13b, the actual response is just slightly stiffer in general, but the form of the response curves is not affected significantly. In total, post-evaluation with body fitted meshes has demonstrated that the proposed method leads to designs that can actually reproduce the target response with very satisfactory accuracy. It only remains to examine in future work, how sensitive these designs are with regard to manufacturing errors.

4. Conclusion

This work has successfully employed third medium contact topology optimization for the inverse design of complex elastomer springs for both stiffening and softening target responses, in both tension and compression. Compared to the previous versions of the topology optimization framework, [15], several improvements have been introduced, leading to faster convergence and designs of higher quality: (1) a simpler version of the void regularization term, (2) B-spline basis functions for the level-set design variable and a very weak penalization of the level-set field curvature, and (3) optional robust formulation (necessary only in very few examples). These modifications have allowed to run all optimization examples until full convergence. All final designs reported, correspond to exact saddle points of the overall monolithic system of equations, equivalent to a fully converged simultaneous analysis and design (SAND) optimization.

Similar to previous works, an objective function was considered which consists of a squared distance sum with respect to a target path, and a weak penalization of utilized material volume. The obtained designs constitute a novel result, as they both account for internal collisions and in most of the cases actually also leverage internal contact in order to achieve the target response. Moreover, examples have been presented both for plane strain and axisymmetric spring designs. Post-evaluation has clearly demonstrated that the inaccuracies introduced due to intermediate densities at the void-solid interface do not affect the validity of the optimized designs considerably.

All examples included resemble axially loaded springs, but an application of the method for the inverse design of periodic material microstructures is a natural and rather straightforward next step. Another important aspect for future work is to include stress or strain constraints in order to avoid excessive deformations involved in some of the designs of the present work.

Declaration of competing interest

The authors declare that they have no known competing financial interests or personal relationships that could have appeared to influence the work reported in this paper.

Data availability

Data will be made available on request.

Acknowledgments

This work was sponsored by the Independent Research Fund Denmark through the Project "TopCon" (grant 1032-00228B).

Appendix A. Demonstration of robust formulation

For the examples with a softening target response under tension (cases T1 and T2), it was observed that, unless a robust formulation is used, non-physical designs are obtained. It seems that strain localization in an intermediate density material region is the most material-efficient albeit non-physical way of achieving a softening response. Such designs can be seen, in their undeformed and deformed configurations, in columns 2–4 of Fig. 14.

Adding one extra control point for a dilated design at 20% tension, although with a much smaller weight in the objective function, eliminates these artifacts. Due to additional material, the dilated design is in general expected to have a larger reaction force at the new control point, deviating significantly from the target value. Nevertheless, this deviation is much smaller for some designs than others. This is the case for the designs shown in the first column, which were obtained after the squared distance for the deviation of the dilated design has been included in the objective, constituting a robust formulation. The respective load–displacements curves, shown in the last column of Fig. 14, demonstrate that the blueprint design obtained with the robust formulation still meets the target as good as the non-robust design but it is free of intermediate density regions.

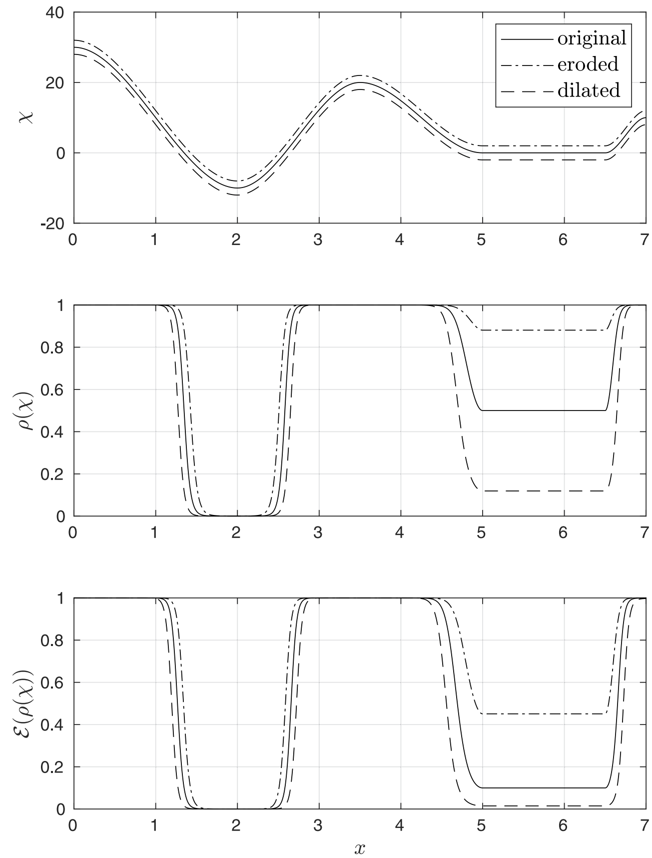

Fig. 15. Simplified illustration of the effect of erosion and dilation on the material stiffness distribution.

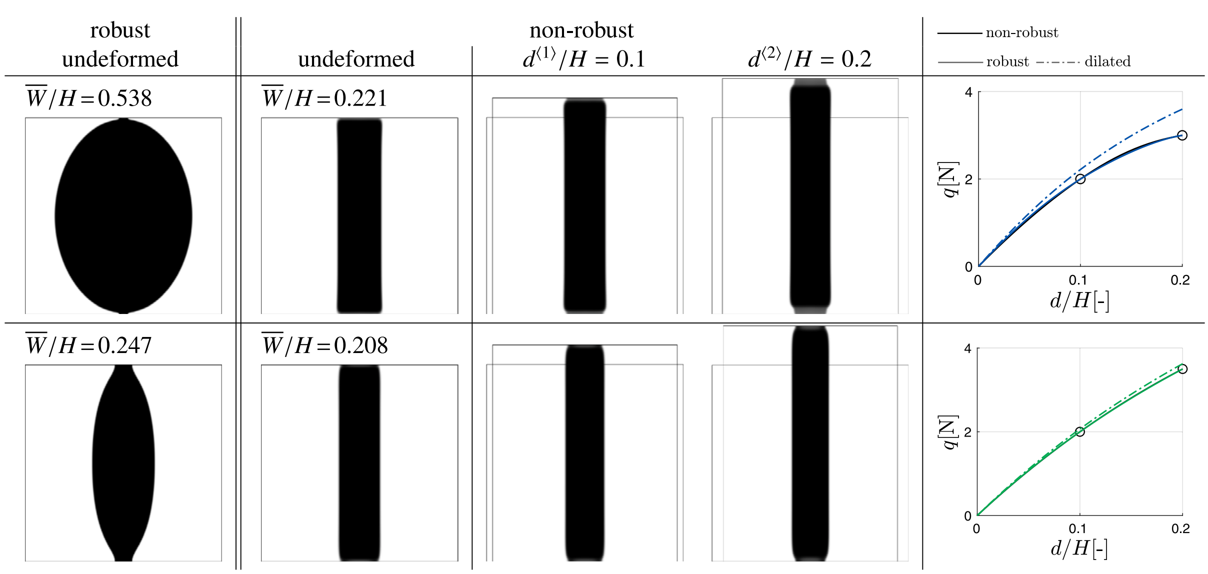

Fig. 14. Tension spring designs obtained with and without the robust formulation for a softening target response.

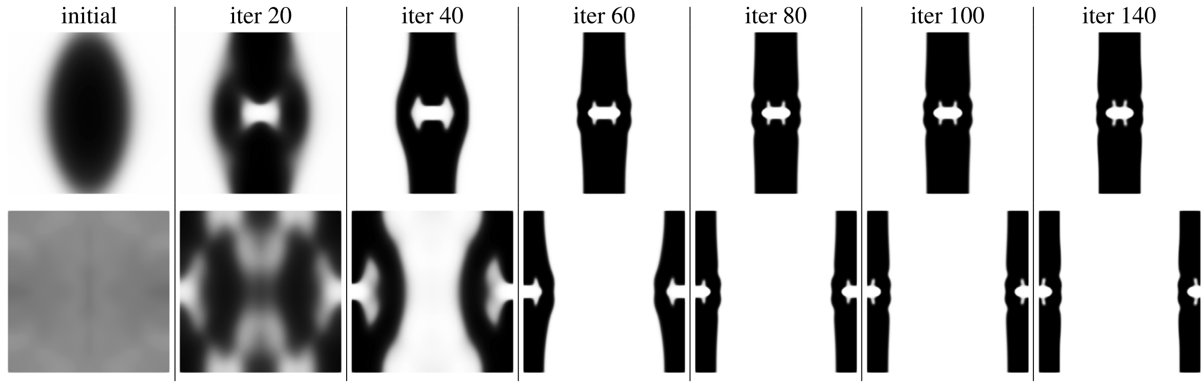

Fig. 16. Optimization convergence history for case C7, starting with the regular initial design in the first row, cf. Fig. 2, and starting with a random design in the second row of images.

The working principle of the robust formulation is further illustrated in Fig. 15. The first plot shows an arbitrary example of the level-set design variable χ along a single dimension x. In regions where χ is clearly positive, the density field ρ, shown in the second plot, is close to 1, and in regions where χ is clearly negative, ρ is close to 0. This example also includes an intermediate density region with $\chi \approx 0$, i.e. $\rho \approx 0.5$. A constant shift in χ, results depending on the direction in either an eroded or a dilated design. For both cases, the third plot illustrates the effect of erosion or dilation on material stiffness, in terms of the RAMP factor $\mathcal{E}(\chi)$. It demonstrates how dilation of intermediate density regions, as those found in the non-robust designs from Fig. 14, will have a large impact on the stiffness in such regions, hence suppressing strain localization which is exploited in the blueprint design.

Appendix B. Optimization with alternative initial designs

As for most topology optimization problems, it is unavoidable that the final optimized design will depend on the initial design that the optimization starts with. The optimality condition, solved for during the optimization process, ensures only a local minimum of the objective function. Depending on the initial design, different local minima may be reached, especially for problems with strong nonlinearities, like the problems involving contact, treated in the present work. In order to provide an indication about the sensitivity of the solution to the initial design, case C7 has been recomputed starting with an alternative random initial design.

Fig. 16 shows the two alternative initial designs, in the first column, and six snapshots during the entire optimization history, in subsequent columns. The first row of images show the optimization history for the result presented in Section 3.1, while the second row of images show the corresponding design iterations when starting with the random design. The random initial design was generated by perturbing a zero level-set field χ with random perturbations defined on uniform 4×4, 8×8, and 12×12 meshes over the problem domain. For each element of the three meshes, uniformly random perturbation values were defined within ±0.4, ±0.222, and ±0.154, respectively, then interpolated to the actual 80×80 mesh with quadratic B-spline interpolation, and superimposed together. Moreover, double mirror symmetry has been enforced.

For the optimization starting with the random design, two halves of a column emerge at the left and right borders of the domain. The boundary conditions on these borders act as a symmetry line, making this split column equivalent to the original one. When the two halves are put together to form a column, the resulting design is strikingly similar to the original one despite the different starting guess and position in the design domain. This confirms that an efficient local optimum has been reached by both designs. The quantitative performances differ slightly, with a volume-equivalent width $\overline{W} = 0.2539H$ reached for the regular initial design, and $\overline{W} = 0.2515H$ for the random initial design, while a number of 153 and 140 iterations were respectively required for full convergence.

Appendix C. Supplementary data

Supplementary material related to this article can be found online at https://doi.org/10.1016/j.ijnonlinmec.2023.104552.

References

[1] Z. Satterfield, N. Kulkarni, G. Fadel, G. Li, N. Coutris, M.P. Castanier, Unit cell synthesis for design of materials with targeted nonlinear deformation response, J. Mech. Des. Trans. ASME 139 (12) (2017) 121401, http://dx.doi.org/10.1115/1.4037894.

[2] R. Behrou, M.A. Ghanem, B.C. Macnider, V. Verma, R. Alvey, J. Hong, A.F. Emery, H.A. Kim, N. Boechler, Topology optimization of nonlinear periodically microstructured materials for tailored homogenized constitutive properties, Compos. Struct. 266 (2021) 113729, http://dx.doi.org/10.1016/j.compstruct.2021.113729.

[3] F. Wang, O. Sigmund, J.S. Jensen, Design of materials with prescribed nonlinear properties, J. Mech. Phys. Solids 69 (1) (2014) 156–174, http://dx.doi.org/10.1016/j.jmps.2014.05.003.

[4] F. Wang, Systematic design of 3D auxetic lattice materials with programmable Poisson's ratio for finite strains, J. Mech. Phys. Solids 114 (2018) 303–318, http://dx.doi.org/10.1016/j.jmps.2018.01.013.

[5] M. Wallin, D.A. Tortorelli, Nonlinear homogenization for topology optimization, Mech. Mater. 145 (2020) 103324, http://dx.doi.org/10.1016/j.mechmat.2020.103324.

[6] T. Buhl, C.B.W. Pedersen, O. Sigmund, Stiffness design of geometrically nonlinear structures using topology optimization, Struct. Multidiscip. Optim. 19 (2) (2000) 93–104.

[7] T.E. Bruns, D.A. Tortorelli, Topology optimization of non-linear elastic structures and compliant mechanisms, Comput. Methods Appl. Mech. Engrg. 190 (26–27) (2001) 3443–3459, http://dx.doi.org/10.1016/S0045-7825(00)00278-4.

[8] C.B.W. Pedersen, T. Buhl, O. Sigmund, Topology synthesis of large-displacement compliant mechanisms, Internat. J. Numer. Methods Engrg. 50 (12) (2001) 2683–2705.

[9] Y. Li, K. Saitou, N. Kikuchi, Topology optimization of thermally actuated compliant mechanisms considering time-transient effect, Finite Elem. Anal. Des. 40 (11) (2004) 1317–1331, http://dx.doi.org/10.1016/j.finel.2003.05.002.

[10] D. Ruiz, O. Sigmund, Optimal design of robust piezoelectric microgrippers undergoing large displacements, Struct. Multidiscip. Optim. 75 (1) (2018) 71–82, http://dx.doi.org/10.1007/s00158-017-1863-5.

[11] C.V. Jutte, S. Kota, Design of nonlinear springs for prescribed load-displacement functions, J. Mech. Des. Trans. ASME 130 (8) (2008) 081403, http://dx.doi.org/10.1115/1.2936928.

[12] W. Li, F. Wang, O. Sigmund, X. Shelly Zhang, Design of composite structures with programmable elastic responses under finite deformations, J. Mech. Phys. Solids 151 (2021) 104356, http://dx.doi.org/10.1016/j.jmps.2021.104356.

[13] W. Li, Y. Jia, F. Wang, O. Sigmund, X.S. Zhang, Programming and physical realization of extreme three-dimensional responses of metastructures under large deformations, Internat. J. Engrg. Sci. (ISSN: 0020-7225) 191 (2023) 103881, http://dx.doi.org/10.1016/j.ijengsci.2023.103881.

[14] P. Wriggers, J. Schröder, A. Schwarz, A finite element method for contact using a third medium, Comput. Mech. 52 (4) (2013) 837–847, http://dx.doi.org/10.1007/s00466-013-0848-5.

[15] G.L. Bluhm, O. Sigmund, K. Poulios, Internal contact modeling for finite strain topology optimization, Comput. Mech. 67 (4) (2021) 1099–1114, http://dx.doi.org/10.1007/s00466-021-01974-x.

[16] A.H. Frederiksen, O. Sigmund, K. Poulios, Topology optimization of self-contacting structures, Comput. Mech. (2023) http://dx.doi.org/10.1007/s00466-023-02396-7, InPress.

[17] M. Stolpe, K. Svanberg, An alternative interpolation scheme for minimum compliance topology optimization, Struct. Multidiscip. Optim. 22 (2) (2001) 116–124, http://dx.doi.org/10.1007/s001580100129.

[18] A. Klarbring, B. Torstenfelt, ODE approach to topology optimization, 8th World Congress on Structural and Multidisciplinary Optimization, Lisbon, Portugal, 2009, p. 1148.

[19] G.L. Bluhm, K. Christensen, K. Poulios, O. Sigmund, F. Wang, Experimental verification of a novel hierarchical lattice material with superior buckling strength, APL Mater. (ISSN: 2166-532X) 10 (9) (2022) 090701, http://dx.doi.org/10.1063/5.0101390.

[20] J.C. Simo, R.L. Taylor, K.S. Pister, Variational and projection methods for the volume constraint in finite deformation elasto-plasticity, Comput. Methods Appl. Mech. Engrg. 51 (1–3) (1985) 177–208, http://dx.doi.org/10.1016/0045-7825(85)90033-7.

[21] D.S. Ebert, F.K. Musgrave, D. Peachey, K. Perlin, S. Worley, W.R. Mark, J.C. Hart, Texturing and Modeling: A Procedural Approach, third ed., Elsevier Inc., 2003, pp. 1–687.

[22] O. Sigmund, Manufacturing tolerant topology optimization, Acta Mech. Sin. 25 (2) (2009) 227–239, http://dx.doi.org/10.1007/s10409-009-0240-z.

[23] F. Wang, B.S. Lazarov, O. Sigmund, On projection methods, convergence and robust formulations in topology optimization, Struct. Multidiscip. Optim. 43 (6) (2011) 767–784, http://dx.doi.org/10.1007/s00158-010-0602-y.

[24] Y. Renard, K. Poulios, GetFEM: Automated FE modeling of multiphysics problems based on a generic weak form language, ACM Trans. Math. Software (ISSN: 0098-3500) 47 (1) (2020) http://dx.doi.org/10.1145/3412849.

[25] C. Geuzaine, J.F. Remacle, GMSH: A 3-D finite element mesh generator with built-in pre- and post-processing facilities, Internat. J. Numer. Methods Engrg. 79 (11) (2009) 1309–1331, http://dx.doi.org/10.1002/nme.2579.

[26] K. Poulios, Y. Renard, An unconstrained integral approximation of large sliding frictional contact between deformable solids, Comput. Struct. (ISSN: 0045-7949) 153 (2015) 75–90, http://dx.doi.org/10.1016/j.compstruc.2015.02.027.